12 Synthesis of transition metal dichalcogenides

Kyungnam Kang, Siwei Chen, Eui-Hyeok Yang

MECHANICAL ENGINEERING DEPARTMENT, STEVENS INSTITUTE OF TECHNOLOGY, HOBOKEN, NJ, UNITED STATES

12.1 Introduction

Transition metal dichalcogenides (TMDs) are composed of three layers; top and bottom layers of chalcogen atoms and middle layer of transition metal atoms. The bandgap of TMDs (WS_2, MoS_2, WSe_2, and $MoSe_2$) changes from indirect to direct bandgap when the materials are thinning from bulk to monolayer [1–3]. The bandgap energies of TMDs are in the range of 1–2 eV [4–7]. The type II heterojunction can be easily fabricated with TMDs due to their band alignment [8–10]. Similar to a strong light interaction material, monolayer subnanometer thick TMDs can absorb up to 5%–10% of incident light [11]. The TMD monolayer has two inequivalent valleys (K and − K valley) at the corner of a Brillouin zone due to inversion symmetry breaking [12]. The strong spin–orbit coupling and inequivalent valleys lead valley dependent optical selection rule and spin–valley locking [13]. These properties of TMDs allow the materials to be used for various applications such as electronic, optical devices, energy harvest, sensors, and catalysts [14–18]. In this chapter the production methods of TMD thin layer and tailoring of the material properties will be introduced. Furthermore, the pros and cons of each production method will be provided for helping the readers to select the proper method for the purpose.

12.2 Mechanical exfoliation

The mechanical exfoliation method uses mechanical force to isolate layers from bulk crystal. This concept has been used for obtaining the first graphite monolayer called graphene [19]. It is a simple, cost-effective, and applicable method to all types of van der Waals materials. Furthermore, high-quality monolayer can be achieved due to using natural bulk crystals [20]. However, it is a time-consuming and nonscalable method [21]. There are several types of mechanical exfoliation methods, such as Scotch-tape, ball milling, roll milling, gel-assisted exfoliation, metal-assisted exfoliation, and layer-resolved splitting (LRS) method [22–27]. The Scotch-tape, metal-assisted, and LRS method will be introduced here because the

Synthesis, Modelling and Characterization of 2D Materials and their Heterostructures.
DOI: https://doi.org/10.1016/B978-0-12-818475-2.00012-X

Scotch-tape method is a representative method of mechanical exfoliation, and LRS is a very unique method that enables wafer-scale monolayer with mechanical exfoliation. The metal-assisted exfoliation is an intermediate method between mechanical and LRS method.

12.2.1 Scotch-tape method

Novoselov et al. used to isolate two-dimensional (2D) monolayer from bulk crystal for the first time. Fig. 12−1 shows the process of the Scotch-tape method [28]. A bulk crystal of 2D material has been located in the middle of the adhesive tape and is thinning by repeated folding and unfolding of the tape. Then the thinned 2D material layers/tape covers SiO_2 substrate, and uniform pressure is applied to increase the adhesion between SiO_2 substrate and thinned 2D material layers. Finally, the adhesive tape is gently removed to leave monolayers of 2D material on the SiO_2 substrate. Novoselov et al. reported a TMD monolayer for the first time with the Scotch-tape method [29]. They measured the mobility of MoS_2 monolayer, and it was between 0.5 and 3 $cm^2/V\,s$. After the Novoselov's work, this method has been used widely to measure the properties of TMDs due to easy, simple, and low-cost process. Lee et al. characterized different layers of MoS_2 with Raman spectroscopy. They found Raman mode of E^1_{2g} is decreasing with thickness, but A_{1g} is increasing with thickness. The different frequencies between E^1_{2g} and A_{1g} are reducing with thickness [30]. Bertolazzi et al. fabricated suspended MoS_2 monolayer and defined the effective Young's modulus and average breaking strength of 270 ± 100 and 23 GPa, respectively [31]. Mak et al. demonstrated the monolayer MoS_2 has a direct bandgap of 1.88 eV [2]. Radisavljevic et al. improved the mobility of MoS_2 monolayer to 200 $cm^2/V\,s$ and demonstrated a high on/off ratio to be 1×108 [32]. Yin et al. measured 7.5 mA/W of photoresponsivity at a gate voltage of 50 V [33].

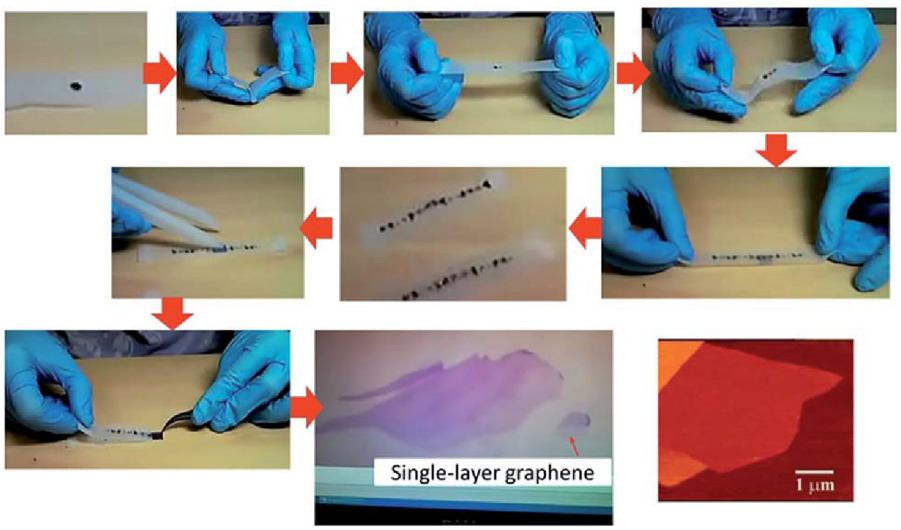

FIGURE 12–1 The procedures of Scotch-tape method to produce monolayer of 2D material. *2D*, Two-dimensional.

12.2.2 Metal-assisted method

Although the Scotch-tape method is a very useful process to obtain monolayer TMDs for property characterization, the production of the large-area monolayer is still challenging with the method. The metal-assisted method can provide a larger flake size than that of the Scotch-tape method. For the metal-assisted method the adhesion between metal and TMD is critical, and gold is a proper metal because gold has a strong semicovalent interaction with the top chalcogen atoms layer of TMDs. Desai et al. developed a gold-assisted exfoliation method that combines the deposited gold layer (100−150 nm) with thermal release tape, as shown in Fig. 12−2. The exfoliated monolayer MoS_2 can reach to about 500-μm^2 [27]. Velický et al. did some further study on the mechanism and surface for the gold exfoliation of TMDs [34]. Through the STEM imaging method, they found that the distance between the gold surface and the attached top sulfur atom of MoS_2 was 3.5 Å. This distance is larger than a covalent bond between gold and sulfur (2.2 Å), indicating that the interaction between gold and sulfur atoms was not chemical bond but strong van der Waals. The binding energy between gold and MoS_2 decreases rapidly with the increase of distance, which indicates the pristine gold layer is required for high-quality exfoliation. This also matches the experiments when the gold surface was exposed to air for a longer duration; the transferred MoS_2 has less percentage of a monolayer. Missing gold atoms on the surface was also studied by DFT simulation. The result shows large vacancies in gold surfaces can also reduce the overall binding force between TMD and the assisting gold surface.

12.2.3 Layer-resolved splitting method

Since the Scotch-tape and metal-assisted exfoliation methods are not scalable, researchers put their efforts to improve the lack of wafer-scale size of exfoliation method. Shim et al. have developed a new method called layer-resolved 2D material splitting technique [26]. This technique can isolate a 2-in. wafer size WS_2 monolayer. For this technique, chemical vapor deposition (CVD)-grown WS_2 multilayer on a sapphire substrate was used for the exfoliation subject instead of naturally synthesized bulk crystal. The CVD-grown sample shows an irregular and discontinuous top layer. However, the under layers are uniform and continuous films.

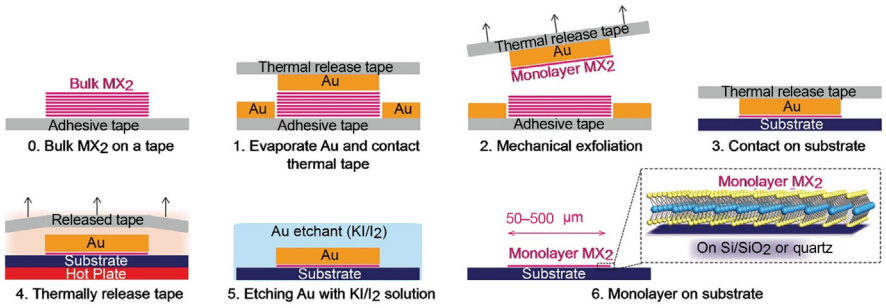

FIGURE 12–2 The illustration of gold-assisted exfoliation process.

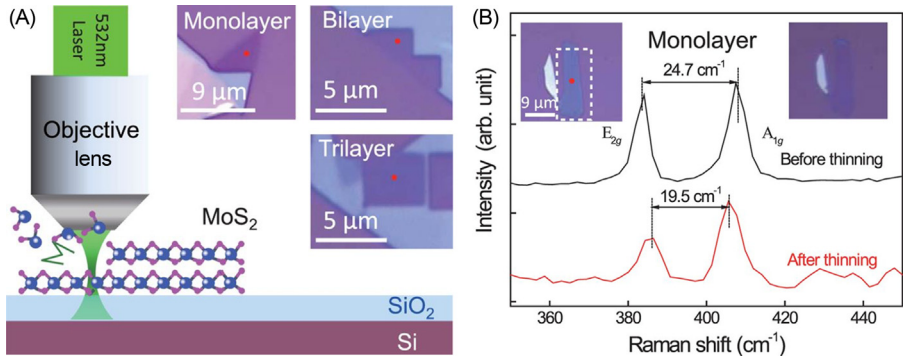

FIGURE 12–3 Laser-assisted thinning of TMD. (A) The device setup and thinning result. (B) Raman measurement of produced monolayer MoS_2. The frequency interval between E^1_{2g} and A_{1g} peaks is 21.0 cm^{-1} indicating its monolayer. The red dot is the position where Raman spectra was collected. *TMD*, Transition metal dichalcogenide.

The WS_2 multilayer has been detached from the sapphire substrate by depositing Ni thick film on top of the multilayer WS_2. Then another thick Ni layer was deposited on the bottom of the multilayer WS_2, and WS_2 monolayer was split from bottom one by one. It is worth mentioning that the quality of the monolayer sample from the LRS method is lower than that of the Scotch-tape method because the LRS method uses CVD-grown samples instead of naturally grown samples.

Here, it is worth introducing the thinning method that removes layers to produce a thin film of TMDs. For the thinning process a few layers of TMD flake is located on a substrate and use thermal energy or laser for the thinning process. Lu et al. applied thermal energy to sublimate TMD flake from the upper layer [35]. In this experiment a laser was produced monolayer TMD by removing extra layers from exfoliated thick TMD. Hu et al. use a 532 nm layer with 2.5 mW with 0.2 second exposure time. After 13 scans the original 10-layer MoS_2 was made into monolayer MoS_2 with a size of around 10 μm [36]. The mechanism behind the laser thinning of TMD multilayer was the thermal thinning when MoS_2 was heated to 603K. While under the laser exposure, the simulation suggests the surface can be around 669K. By controlling the exposure time and power, this method can make bulk MoS_2 into the desired thickness. This method can fabricate the square pattern of MoS_2 trilayer, bilayer, and monolayer from bulk material (Fig. 12−3A). The thickness of MoS_2 was confirmed by Raman measurements, as the frequency interval between E^1_{2g} and A_{1g} Raman peaks is around 25.3 cm^{-1} for bulk and 19.4 cm^{-1} for monolayers [37] (Fig. 12−3B). Unlike other exfoliation and thinning methods, this method comes with location and structure control of monolayer TMD. This method has potential application in novel devices with structural design.

12.3 Liquid-phase exfoliation

The liquid-phase exfoliation is a very useful method to achieve large-scale and mass production of 2D materials at low cost for various applications. Furthermore, 2D materials can be

deposited on a variety of substrates because the process can be done at low temperatures. Those advantages of this method are useful for thin-film transistors, inkjet-printed electronics, conductive electrodes, and nanocomposites [38−41]. The liquid-phase exfoliation has clear drawbacks such as small grain size, high defect density, high possibility of contamination by chemical groups, and possible phase transition of exfoliated TMDs. Although several liquid-phase exfoliation methods have been reported, solvent-based and ion intercalation methods are the two most popular methods [42,43].

12.3.1 Solvent-based exfoliation method

The procedure of the solvent-based exfoliation method consists of immersion, insertion, exfoliation, and stabilization. Fig. 12−4 is the schematic diagram of the procedures of solvent-based exfoliation. The solvents must fully immerse the 2D material for providing efficient exfoliation during sonication. Furthermore, they need to exfoliate the material at high concentration and keep from the restacking of exfoliated 2D material. To satisfy the conditions, surface tension, Hildebrand, and Hansen solubility parameters must be taken into consideration to decide the proper solvent for a given 2D material. Based on the solvent requirements, IPA/water, acetone/water, and THF/water are the best well-known solvents. The optimal volumetric ratio of solvent to water depends on 2D material. Shen et al. suggested a 1:1 IPA/water ratio for graphene, hBN, WS_2, and $MoSe_2$ and 7:3 for MoS_2 [42].

12.3.2 Ion intercalation method

The fundamental principle behind the ion intercalation method is the intercalation of impurities between layers of bulk TMD crystal to increase the interlayer space. Then the increased

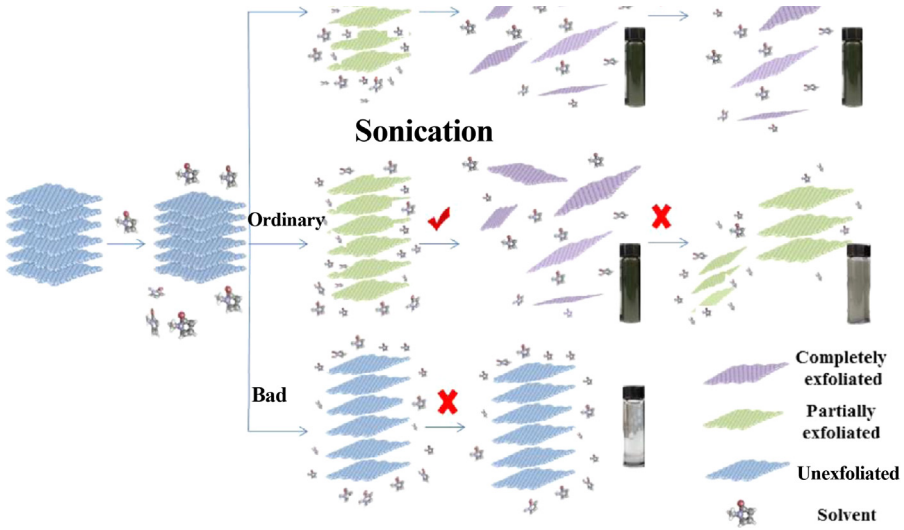

FIGURE 12–4 The schematic illustration of solvent-based exfoliation method.

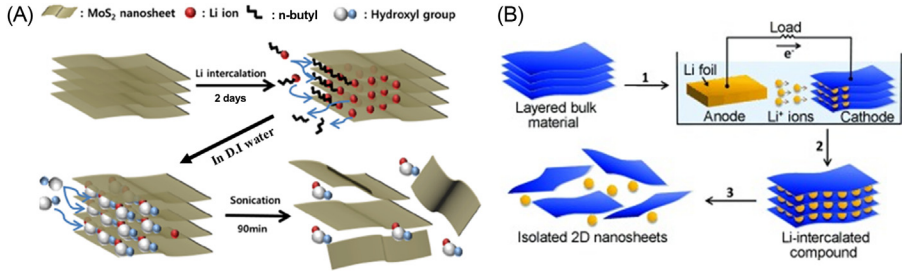

FIGURE 12–5 The schematic diagram of ion intercalation method: (A) lithium intercalation and exfoliation process and (B) electrochemical lithium intercalation and exfoliation process for TMD material. *TMD*, Transition metal dichalcogenide.

interlayer space reduces van der Waals force with the energy barrier to exfoliation. The intercalants include alkali metal, organometallic, polymers, and atomic species. Lithium-ion is a good material because of its high reduction potential and high mobility. For lithium intercalation, *n*-butyllithium (*n*-BuLi) solution in hexane has been widely used. The *n*-Bu^- transfers an electron to TMD layers and Li^+ ion intercalates for the charge balance. Ultrasonication or microwaves have been used to improve lithium intercalation efficiency. The lithium-ion-intercalated TMD bulk crystal is exfoliated by hydrolyzing and sonication. Fig. 12−5A is an illustration of a lithium-intercalated exfoliation process [44]. Zeng et al. introduced the advanced Li-ion intercalation method by using the electrochemical approach (Fig. 12−5B). The lithium intercalation of the electrochemical approach is faster and controllable method [43]. For the lithium intercalation process, a voltage was applied between anodic lithium foil and cathodic bulk TMD in an electrolyte. During the process, the Li^+ ions are placed between the TMD layers. The Li^+ ion-intercalated TMD bulk crystal is agitated to generate TMD nanosheets. This exfoliation process can lead to structural deformation of the exfoliated material. The lithium intercalation is associated with charge transfer from *n*-BuLi to the TMD crystal, and the charge transfer changes the structure of TMD from 2 H to 1 T [45]. This phase change is more favorable when the lithium dosage is increasing. However, this intercalation-induced phase transformation is reversible by annealing process or exposing to infrared (IR) radiation [46,47].

12.4 Chemical vapor deposition

The CVD method for monolayer 2D material growth was first reported in 2007 for graphene growth [48]. Since then, the CVD method has improved due to its cost-effective and scalable production. Now it is the most popular method for the growth of 2D materials because it can manipulate growth location, the number of layers, grain size, and doping impurities in addition to large-scale growth [49−57]. In this section, three different types of CVD methods will be described for TMD growth: thermal CVD, metal oxide CVD (MOCVD), and chemical vapor transport (CVT) methods.

12.4.1 Thermal chemical vapor deposition

Before discussing the thermal-CVD growth mechanism of TMD monolayer, it is worth noting the difference in the thermal-CVD growth mechanism between graphene and TMDs. For the growth of graphene with a thermal-CVD method, the introduced hydrocarbon gases are decomposed on the surface of the metal substrate, and carbon atoms dissolve into the substrate. The carbon atoms segregate and form a graphene layer during the cooling down of the substrate due to the solubility difference according to the temperature. Thus thin metal foils have been used as a substrate because the carbon solubility of the substrate is key for the graphene growth [58–60]. Unlike the formation process of graphene, the chemical reaction between precursors is the main route for the synthesis of TMDs. In general, powder forms of transition metal oxide and chalcogen are used as precursors. The precursors will evaporate at high temperatures and adsorb on a substrate where the chalcogenization of transition metal oxide occurs to form TMDs [61–63]. Imanishi et al. deposited MoS_2 film with a thermal-CVD method in 1992 [64], and Lee et al. grew MoS_2 monolayer on a SiO_2 substrate in 2012 [65]. They have used MoO_3 powder and sulfur powder as precursors. Nitrogen gas has been used as a carrier gas. The SiO_2 substrate has been treated with reduced graphene oxide, perylene-3,4,9,10-tetracarboxylic acid tetrapotassium salt (PTAS), or perylene-3,4,9,10-tetracarboxylic dianhydride (PTCDA) to promote MoS_2 monolayer growth. Fig. 12–6 is a diagram of a typical thermal-CVD setup for TMD growth [66].

The transition metal oxide and chalcogen powder are located at different temperature zones due to the difference in the sublimation temperature. Therefore the thermal-CVD furnace, which has two independent heating zones, is better to control the evaporation moment of the precursors. The transition metal oxide is in a higher temperature zone than chalcogen to evaporate both precursors at the same time. The gas-phase of transition metal oxide is adsorbed on the substrate, and chalcogen gas is delivered to the substrate surface by an inert carrier gas (Ar or N). The TMD monolayer is formed on the substrate surface after the chalcogenization of preadsorbed transition metal oxide. Hydrogen gas occasionally is introduced to improve the reduction of transition metal oxide resulting in better chalcogenization [67]. The typical growth temperatures are between 750°C and 950°C. Fundamental experiments show the relationship between the ratio of transition metal (M) to chalcogen (X), growth

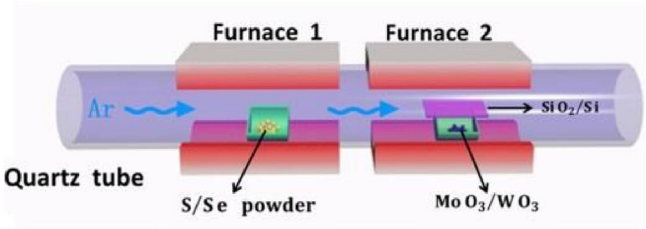

FIGURE 12–6 An illustration of typical thermal CVD setup for TMD growth. *CVD*, Chemical vapor deposition; *TMD*, transition metal dichalcogenide.

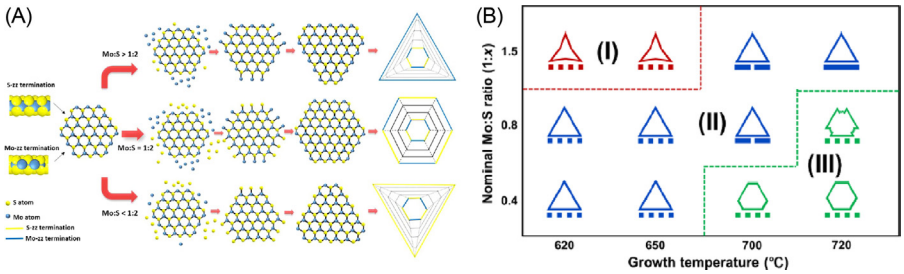

FIGURE 12–7 An illustration of domain shape and growth parameters: (A) the shape of domain according to the M:X ratio and (B) the shape of domain with respect to the nominal M:X ratio and growth temperature.

temperature, edge structure, and shape evolution of TMDs as shown in Fig. 12−7A. Wang et al. demonstrated that the crystal domain will have M zigzag edge and triangle shape if the M:X ratio is greater than 1:2. If the M:X ratio is less than 1:2, the domain will have X zigzag edge and triangle shape. When the M:X ratio is equal to 1:2, the domain will have an alternative M and X zigzag edge and hexagonal or truncated triangle shape [68]. Yang et al. added one more factor, growth temperature, to a connection between M:X ratio and the shape of the domain. As is shown in Fig. 12−7B, they separated three noticeable growth conditions deciding domain shapes into a three-point star, triangle, and hexagonal flakes [69].

After the nucleation the grain size of TMDs increases and the adjacent grains start to merge. At this moment, the grain would like to stop the growth instead of overlap and keep growing on top of each other. Thus a large area of monolayer TMDs can be grown with a thermal-CVD method. An experimental result recently published shows wafer-scale single-crystalline WS_2 and MoS_2 monolayer have been grown. Lee et al. used single-crystalline hexagonal boron nitride (SC-hBN) grown by using self-collimation of B and N edges inherently. They used sodium tungstate dihydrate ($Na_2WO_4 \cdot 2H_2O$) dissolved in acetylacetone as a W precursor, sodium molybdate dihydrate ($Na_2MoO_4 \cdot 2H_2O$) in acetylacetone as a Mo precursor, liquid ammonium sulfide solution ($(NH_4)_2S$) as an S precursor, and carrier gases of H_2 and Ar. The triangle shape of WS_2 and MoS_2 monolayers had been grown all over the substrate with aligned direction. The prolonged growth time leads to wafer size single-crystalline WS_2 and MoS_2 monolayer [70].

12.4.2 Metalorganic chemical vapor deposition (MOCVD)

The TMD growth method for scale-up production is critical for commercialization, and MOCVD is a good technique for it. Although MOCVD is a relatively recently developed growth method for TMDs, it is an already well-known method for the deposition of thin-film semiconductors [71−73]. For the growth of TMD with the MOCVD method, gases of organic molecules containing transition metal (Mo or W) and chalcogen (S or Se) are introduced over a substrate and decomposed by thermal energy to deposit TMD thin film on the substrate. Especially, the MOCVD method can control the partial pressure of the precursors

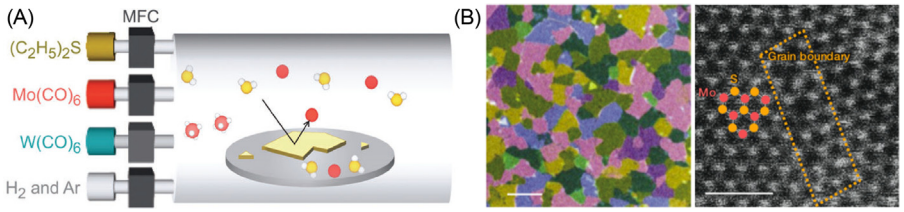

FIGURE 12–8 (A) Schematic diagram of MOCVD setup and (B) false-color TEM image of MoS_2 monolayer. Scale bar is 1 μm. STEM image of stitched grain boundary.

precisely. Thus this technique allows for uniform deposition of TMDs on the large size of a substrate. Fig. 12−8A is the schematic diagram of a typical MOCVD setup [74].

Kang et al., deposited uniform monolayer and few layers of MoS_2 and WS_2 on 4-in. SiO_2 substrate by using molybdenum hexacarbonyl [$Mo(CO)_6$], tungsten hexacarbonyl [$W(CO)_6$], ethylene disulfide [$(C_2H_5)_2S$], Ar, and H_2 [74]. The Ar has been used as a carrier gas and H_2 is improving grain size and crystalline quality. Eichfeld et al. synthesized WSe_2 thin film on various substrates. They have demonstrated the temperature, pressure, transition metal to chalcogen ratio, and substrate effect for the morphology of the film [75]. The TEM image shows the size of grain and well-stitched grain boundaries in Fig. 12−8B [74]. The average grain size is around 1 μm, and they have claimed that larger grain size can be obtained under high pressure, growth temperature, and Se:W ratio. This growth process needs 26 hours to synthesis a 4-in. MoS_2 monolayer. The slow growth rate needs to be improved, and Kalanyan et al. reported much-improved deposition rate. They deposited a few layers of MoS_2 films in 90 seconds by using a pulsed MOCVD method with bis(tert-butylimido)-bis (dimethylamido)molybdenum and diethyl disulfide precursors [76].

The MOCVD method can control the number of layers and grow uniform film on a large area, but it needs toxic precursors and high-cost equipment. It provides a small grain size, but with a proper condition, this method can produce a wafer-scale homogeneity monolayer.

12.4.3 Chemical vapor transport method

The concept of the CVT method was invented in the middle of the 19th century for the growth of single-crystal materials. Schafer conducted systematic research of CVT and elaborated on the migration process. Fischer et al. employed sealed ampoule for the first time. Fig. 12−9A shows a setup of a typical CVT method [77].

A powder form of precursor (AB(s)) is in the source zone (high temperature) with a gas form of transport agent (L(g)). The evaporated precursor is going to decompose and react with the transporting agent. Then, the gases move to the low-temperature area, which is called the sink or deposition zone. The reverse reaction occurs at the deposition zone resulting in the reformation of a single-crystalline structure.

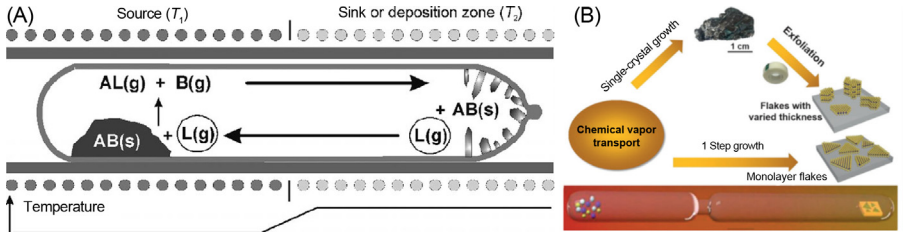

FIGURE 12–9 Illustration of a typical CVT system. TMD growth with CVT method. *CVT*, chemical vapor transport; *TMD*, transition metal dichalcogenide.

As shown in Fig. 12−9B, there are two different routes to obtain TMD monolayer with CVT [78]. One is the exfoliation process with a bulk crystal of TMD, which is grown with the CVT method, and the other is growing TMD monolayer on a substrate located at the deposition zone in the ampoule. Dave et al. synthesized MoS_2 and $MoSe_2$ bulk crystal with the CVT method. They used Mo, S, and S_2 as precursors and I_2 as a transporting agent [79]. Interestingly, both crystals show p-type, unlike CVD samples, show n-type. Ubaldini et al. demonstrated a chloride-driven CVT method to grow MoS_2, $MoSe_2$, and $MoTe_2$ bulk crystals [80]. They used Mo, S, Se, and Te with $MoCl_5$. They found the ratio of transition metal to transition metal chloride is an important parameter, and the ratio depends on the atomic number of chalcogen, such as 50 for sulfide and 15 for telluride. Hu et al. deposited MoS_2 monolayer on a mica substrate. MoO_3 and S were used precursors, and I_2 was used for transport agents [78]. This process allows avoiding the mechanical exfoliation process for obtaining monolayer MoS_2 after bulk MoS_2 crystal growth with CVT. CVT provides high-quality TMD samples that are comparable to that of a mechanical exfoliated sample, but the experimental preparation is complicated and laborious.

12.5 Molecular-beam epitaxy

The use of molecular-beam epitaxy (MBE) in semiconductor devices fabrication can be traced back to the 1960s. The deposition requires an ultrahigh vacuum (UHV) that typically goes below 10^{-8}−10^{-12} Torr [81]. During MBE epitaxial film growth, the molecular source was provided from effusion cells by heating the solid material or providing the gas source. During the generation of molecular source, no chemical reaction was involved, the chemical reaction was taking place on the target substrate (Fig. 12−10A) [82,83]. By controlling the shutters of individual effusion cells, MBE can make a sharp atomically thin layer between epitaxy layers or doping the epitaxy layer precisely. Another advantage of using MBE is the UHV environment can produce high purity of grown films.

MBE is one of the first scalable methods for TMD monolayer fabrication. Start from 1980s, Koma synthesized monolayer $MoSe_2$ on $CaF_2(111)$ substrate [84]. Since the doping of TMD can be achieved by introducing an extra molecular-beam source, MBE has the potential for fabricating heterostructure with a doped layer. Fu et al. have achieved MoS_2

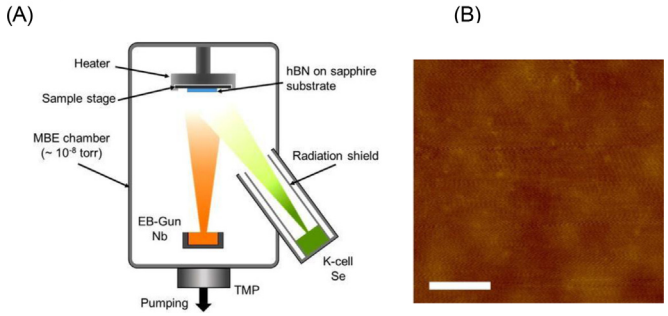

FIGURE 12–10 (A) The schematic diagram of typical MBE deposition system, and (B) AFM image of MBE grown MoS_2 monolayer. Scale bar is 200 nm. *MBE*, Molecular-beam epitaxy; *TMD*, transition metal dichalcogenide.

monolayer on hBN [85]. Fig. 12−10B shows an AFM image of seamless MoS_2 monolayer grown on an hBN/sapphire wafer. This method can provide wafer-scale TMD monolayer, but it takes around 10 hours to grow 2-in. wafer size of MoS_2 monolayer and needs expensive effusion equipment [83,85].

12.6 Doping/alloy of transition metal dichalcogenides

Although TMDs have been widely studied for the applications due to the inherent optical and electrical properties, the tailoring of the material property allows better material selection for specific applications and improves the performance of devices. Several methods for the manipulation of TMD properties are available, and doping is one of the methods. The doping method can be subcategorized, such as substitutional, interstitial, and charge doping [54,86−90]. Here, the substitutional doping will be considered. The substitutional doping represents the impurity atoms to replace host atoms to form covalent bonds. Thus the products are stable, and property degradation is smaller than that of other doping types [91]. The TMDs consist of cation elements of the transition metal (Mo and W) and anion elements of chalcogenide (S and Se). Thus two different types of cation and anion substitutional doping will be considered.

12.6.1 Substitution of cation elements in transition metal dichalcogenides

The cation substitutional doping is a method where the host atoms of transition metal in TMD are replaced by the impurity atoms. The tungsten doping on Mo-based TMDs and vice versa are well-known cation substitution processes to manipulate the optical properties. The TMDs have their own peak value of photoluminescence (PL), and the peak position can be shifted by substitutional doping of transition metal atoms and chalcogen atoms. Fig. 12−11A is the graph of PL intensities of WS_2, MoS_2, WSe_2, and $MoSe_2$ monolayers on SiO_2 substrate

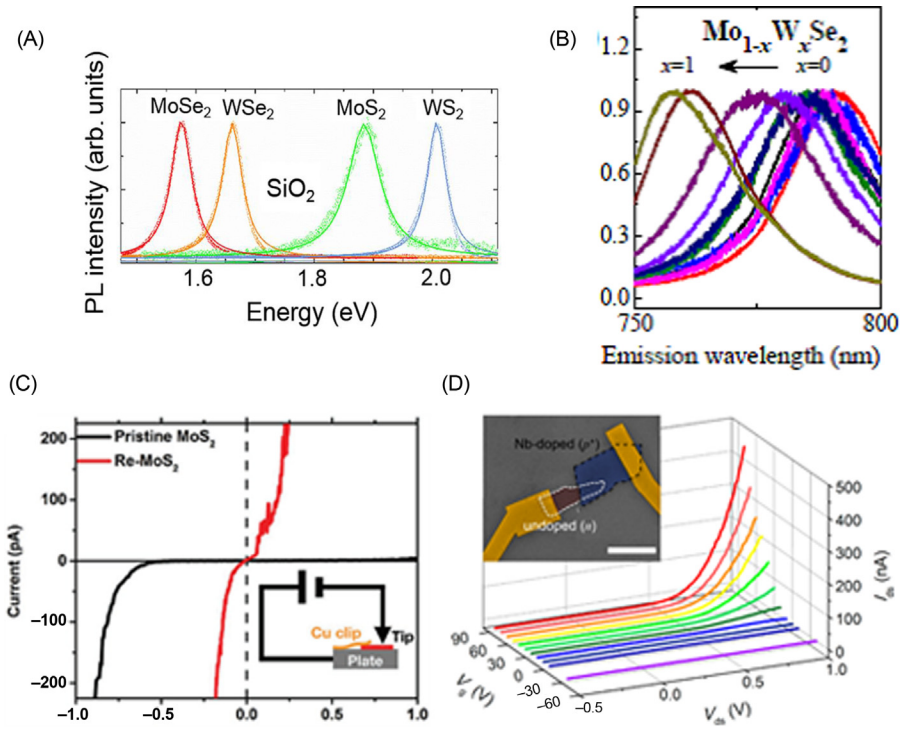

FIGURE 12–11 (A) The normalized photoluminescences of TMDs that represent bandgap of the material; (B) normalized photoluminescences of $Mo_{1-x}W_xSe_2$ alloy with different x ($0 \le x \le 1$) values; (C) the $I-V$ curve of pristine and Re-doped MoS_2 monolayer, the Re-doped MoS_2 monolayer shows more close to metal than semiconductor; and (D) Nb-doped MoS_2 monolayer gives ohmic contact and shows p-type behavior. The fabricated p−n homojunction shows current rectification. *TMDs*, Transition metal dichalcogenides.

at room temperature [92]. The PL peaks are 2.03, 1.88, 1.67, and 1.57 eV for WS_2, MoS_2, WSe_2, and $MoSe_2$ respectively [93]. Tongay et al. control the concentration of W and Mo to fabricate $Mo_{1-x}W_xSe_2$ monolayer for tuning the PL peak in Fig. 12−11B [94]. Other metal atoms have been used for the cation substitutional doping to tailor the property. Rhenium (Re) has been used for donor acting as an n-type dopant, and Niobium (Nb) has been used for acceptor acting as p-type dopants. Zhang et al. doped MoS_2 with Re and shifted the Fermi level up by 0.5 eV resulting in degenerate n-type doping [95]. The $I-V$ curve of doped and undoped MoS_2 monolayer has been measured with conductive atomic force microscopy (CAFM) tip. Fig. 12−11C indicates a Schottky barrier junction between the CAFM tip and pristine MoS_2 [95]. However, the behavior of Re-doped MoS_2 is more close to metal instead of a semiconductor. Suh et al. use Nb as a p-type dopant to transit from inherently n-type MoS_2 to extrinsic p-type doped MoS_2. The 0.5% Nb doping concentration gives ohmic contact between the doped MoS_2 and the Ti electrode instead of the expected Schottky barrier. The p−n homojunction of vertically stacked Nb-doped and undoped MoS_2 shows gate tunable current rectification in Fig. 12−11D [96].

12.6.2 Substitution of anion elements in transition metal dichalcogenides

The anion substitutional doping is a technique for replacing host atoms of chalcogenides in TMD by nonmetal dopants. Li et al. grew Se-doped MoS_2 monolayer ($MoS_{2x}Se_{2-2x}$) with different Se concentration [97]. As shown in Fig. 12−12A, the PL peak changes from 659 to 789 nm according to the Se concentration. The transition from WS_2 to WSe_2 by substitutional doping of Se on WS_2 monolayer changes not only the energy of PL peak but also the semiconductor type from n- to p-type. The WS_2, MoS_2, and $MoSe_2$ show inherently n-type semiconductor property, but WSe_2 show a p-type property. Thus the transition from WS_2 to WSe_2 changes not only the PL peak position but also semiconductor type from n- to p-type. Duan et al. measured PL intensity and threshold voltages of $WS_{2x}Se_{2-2x}$ with a different value of x. Fig. 12−12B and C shows the PL changes and p-type in WSe_2 and n-type in WS_2 [98]. Yang et al. doped a few layers of WS_2 and MoS_2 with chloride molecules (Cl) as a dopant [99]. As shown in Fig. 12−12D, the Cl-doped WS_2 and MoS_2 reduced contact resistance and Schottky barrier width. Azcatl et al. used nitrogen to replace sulfur atoms of MoS_2. The nitrogen-doped MoS_2 FET in Fig. 12−12E indicates a positive shifted threshold voltage (Vth) that represents nitrogen-doped MoS_2 is a p-type material [100].

The tailoring of TMD property is getting important for better performance of devices and a variety of applications. The substitutional doping of ferromagnetic material on TMDs generates a stable magnetic phase, and the 2D dilute magnetic semiconductors are drawing attention due to the application for spintronic and memory devices.

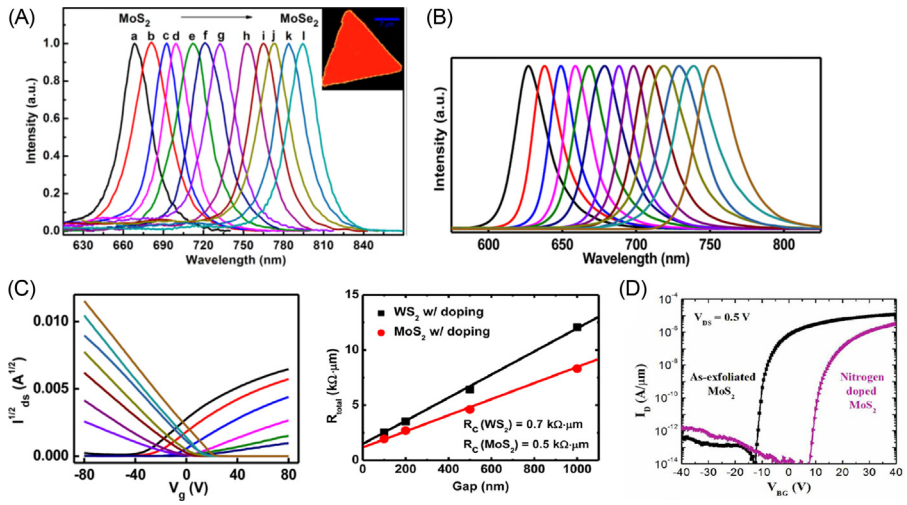

FIGURE 12–12 (A) The normalized photoluminescences of $MoS_{2x}Se_{2-2x}$ alloy with different x ($0 \le x \le 1$) values, (B) normalized photoluminescences of $WS_{2x}Se_{2-2x}$ alloy with different x ($0 \le x \le 1$) values, (C) the $I-V$ curve shows the alloy represents n-type semiconductor when it is WS_2-rich alloy and p-type property when it is WSe_2-rich alloy, (D) chlorine-doped MoS_2 and WS_2 have low contact resistance between Ni and doped material, and (E) the nitrogen-doped MoS_2 changes the type of property from n- to p-type.

12.7 Summary

The TMDs are 2D semiconductor materials showing unique electrical, mechanical, and optical properties. Thus the materials can compensate for graphene (metallic material) and hexagonal boron nitride (hBN, insulator) for the applications of the next-generation semiconductor devices. In this section a variety of TMD growth methods were introduced. Although the basic concepts of production methods can be shared with another van der Waals materials, TMDs need a different approach due to the different compounds and growth mechanisms. Mechanical exfoliation methods use a bulk crystal of TMDs to produce high-quality samples quickly and easily. Remarkably, the LRS method gives wafer-size TMD monolayer by using CVD-grown multilayer TMD on a SiO_2 substrate. Liquid-phase exfoliations provide mass production of pristine few-layer TMDs. Chemical vapor deposition methods can grow wafer-scale TMD monolayer, control the number of TMD layers, manipulate the location of the growth, and manage the grain size of TMDs. Furthermore, doping of the TMDs for tailoring properties has been introduced. The doping processes change bandgap, type, mobility, and contact resistance. In addition, the magnetic properties can be changed by doping.

The knowledge of TMD preparation methods and doping effects can help the reader in choosing an appropriate method for their research applications and directions

References

[1] Y. Zhang, et al., Direct observation of the transition from indirect to direct bandgap in atomically thin epitaxial $MoSe_2$, Nat. Nanotechnol. 9 (2) (2014) 111–115.

[2] K.F. Mak, C. Lee, J. Hone, J. Shan, T.F. Heinz, Atomically thin MoS_2: A new direct-gap semiconductor, Phys. Rev. Lett. 105 (13) (2010) 2–5.

[3] I.G. Lezama, et al., Indirect-to-direct band gap crossover in few-layer $MoTe_2$, Nano Lett. 15 (4) (2015) 2336–2342.

[4] H.J. Conley, B. Wang, J.I. Ziegler, R.F. Haglund, S.T. Pantelides, K.I. Bolotin, Bandgap engineering of strained monolayer and bilayer MoS_2, Nano Lett. 13 (8) (2013) 3626–3630.

[5] W. Zhao, et al., Evolution of electronic structure in atomically thin sheets of WS_2 and WSe_2, ACS Nano 7 (1) (2013) 791–797.

[6] A. Arora, M. Koperski, K. Nogajewski, J. Marcus, C. Faugeras, M. Potemski, Excitonic resonances in thin films of WSe_2: from monolayer to bulk material, Nanoscale 7 (23) (2015) 10421–10429.

[7] M.M. Ugeda, et al., Giant bandgap renormalization and excitonic effects in a monolayer transition metal dichalcogenide semiconductor, Nat. Mater. 13 (12) (2014) 1091–1095.

[8] V.O. Özçelik, J.G. Azadani, C. Yang, S.J. Koester, T. Low, Band alignment of two-dimensional semiconductors for designing heterostructures with momentum space matching, Phys. Rev. B 94 (3) (2016) 035125.

[9] C.-H. Lee, et al., Atomically thin p–n junctions with van der Waals heterointerfaces, Nat. Nanotechnol. 9 (9) (2014) 676–681.

[10] J. Kang, S. Tongay, J. Zhou, J. Li, J. Wu, Band offsets and heterostructures of two-dimensional semiconductors, Appl. Phys. Lett. 102 (1) (2013) 012111.

[11] X. Li, H. Zhu, Two-dimensional MoS_2: properties, preparation, and applications, J. Mater. 1 (1) (2015) 33–44.

[12] H. Zeng, J. Dai, W. Yao, D. Xiao, X. Cui, Valley polarization in MoS_2 monolayers by optical pumping, Nat. Nanotechnol. 7 (8) (2012) 490–493.

[13] D. Xiao, G.-B. Liu, W. Feng, X. Xu, W. Yao, Coupled spin and valley physics in monolayers of MoS_2 and other group-VI dichalcogenides, Phys. Rev. Lett. 108 (19) (2012) 196802.

[14] H. Kwon, et al., Large scale MoS_2 nanosheet logic circuits integrated by photolithography on glass, 2D Mater. 3 (4) (2016) 044001.

[15] O. Lopez-Sanchez, D. Lembke, M. Kayci, A. Radenovic, A. Kis, Ultrasensitive photodetectors based on monolayer MoS_2, Nat. Nanotechnol. 8 (7) (2013) 497–501.

[16] C. Li, et al., Engineering graphene and TMDs based van der Waals heterostructures for photovoltaic and photoelectrochemical solar energy conversion, Chem. Soc. Rev. 47 (13) (2018) 4981–5037.

[17] S. Barua, H.S. Dutta, S. Gogoi, R. Devi, R. Khan, Nanostructured MoS_2-based advanced biosensors: a review, ACS Appl. Nano Mater. 1 (1) (2018) 2–25.

[18] L. Madauß, et al., Highly active single-layer MoS_2 catalysts synthesized by swift heavy ion irradiation, Nanoscale 10 (48) (2018) 22908–22916.

[19] K.S. Novoselov, et al., Two-dimensional gas of massless Dirac fermions in graphene, Nature 438 (7065) (2005) 197–200.

[20] H. Li, J. Wu, Z. Yin, H. Zhang, Preparation and applications of mechanically exfoliated single-layer and multilayer MoS_2 and WSe_2 nanosheets, Acc. Chem. Res. 47 (4) (2014) 1067–1075.

[21] H. Yuan, D. Dubbink, R. Besselink, J.E. ten Elshof, The rapid exfoliation and subsequent restacking of layered titanates driven by an acid-base reaction, Angew. Chemie Int. Ed. 54 (32) (2015) 9239–9243.

[22] H. Li, et al., Rapid and reliable thickness identification of two-dimensional nanosheets using optical microscopy, ACS Nano 7 (11) (2013) 10344–10353.

[23] A.E. Del Rio-Castillo, C. Merino, E. Díez-Barra, E. Vázquez, Selective suspension of single layer graphene mechanochemically exfoliated from carbon nanofibres, Nano Res. 7 (7) (2014) 963–972.

[24] J. Chen, M. Duan, G. Chen, Continuous mechanical exfoliation of graphene sheets via three-roll mill, J. Mater. Chem. 22 (37) (2012) 19625.

[25] P. Budania, et al., Comparison between scotch tape and gel-assisted mechanical exfoliation techniques for preparation of 2D transition metal dichalcogenide flakes, Micro. Nano. Lett. 12 (12), (2017), 970–973.

[26] J. Shim, et al., Controlled crack propagation for atomic precision handling of wafer-scale two-dimensional materials, Science 362 (6415) (2018) 665–670.

[27] S.B. Desai, et al., Gold-mediated exfoliation of ultralarge optoelectronically-perfect monolayers, Adv. Mater. 28 (21) (2016) 4053–4058.

[28] M. Yi, Z. Shen, A review on mechanical exfoliation for the scalable production of graphene, J. Mater. Chem. A 3 (22) (2015) 11700–11715.

[29] K.S. Novoselov, et al., Two-dimensional atomic crystals, Proc. Natl. Acad. Sci. U.S.A. 102 (30) (2005) 10451 LP–10410453.

[30] C. Lee, H. Yan, L.E. Brus, T.F. Heinz, J. Hone, S. Ryu, Anomalous lattice vibrations of single- and few-layer MoS_2, ACS Nano 4 (5) (2010) 2695–2700.

[31] S. Bertolazzi, J. Brivio, A. Kis, Stretching and breaking of ultrathin MoS_2, ACS Nano 5 (12) (2011) 9703–9709.

[32] B. Radisavljevic, A. Radenovic, J. Brivio, V. Giacometti, A. Kis, Single-layer MoS_2 transistors, Nat. Nanotechnol. 6 (3) (2011) 147–150.

[33] Z. Yin, et al., Single-layer MoS_2 phototransistors, ACS Nano 6 (1) (2012) 74–80.

[34] M. Velický, et al., Mechanism of gold-assisted exfoliation of centimeter-sized transition-metal dichalcogenide monolayers, ACS Nano 12 (10) (2018) 10463–10472.

[35] X. Lu, M.I.B. Utama, J. Zhang, Y. Zhao, Q. Xiong, Layer-by-layer thinning of MoS_2 by thermal annealing, Nanoscale 5 (19) (2013) 8904–8908.

[36] L. Hu, X. Shan, Y. Wu, J. Zhao, X. Lu, Laser thinning and patterning of MoS_2 with layer-by-layer precision, Sci. Rep. 7 (1) (2017) 15538.

[37] H. Li, et al., From bulk to monolayer MoS_2: evolution of Raman scattering, Adv. Funct. Mater. 22 (7) (2012) 1385–1390.

[38] F. Torrisi, et al., Inkjet-printed graphene electronics, ACS Nano 6 (4) (2012) 2992–3006.

[39] X. Zeng, H. Hirwa, S. Metel, V. Nicolosi, V. Wagner, Solution processed thin film transistor from liquid phase exfoliated MoS_2 flakes, Solid State Electron. 141 (2018) 58–64.

[40] P. Blake, et al., Graphene-based liquid crystal device, Nano Lett. 8 (6) (2008) 1704–1708.

[41] J. Xiao, D. Choi, L. Cosimbescu, P. Koech, J. Liu, J.P. Lemmon, Exfoliated MoS_2 nanocomposite as an anode material for lithium ion batteries, Chem. Mater. 22 (16) (2010) 4522–4524.

[42] J. Shen, et al., Liquid phase exfoliation of two-dimensional materials by directly probing and matching surface tension components, Nano Lett. 15 (8) (2015) 5449–5454.

[43] Z. Zeng, et al., Single-layer semiconducting nanosheets: high-yield preparation and device fabrication, Angew. Chemie Int. Ed. 50 (47) (2011) 11093–11097.

[44] J.H. Lee, W.S. Jang, S.W. Han, H.K. Baik, Efficient hydrogen evolution by mechanically strained MoS_2 nanosheets, Langmuir 30 (32) (2014) 9866–9873.

[45] S. Shi, Z. Sun, Y.H. Hu, Synthesis, stabilization and applications of 2-dimensional 1T metallic MoS_2, J. Mater. Chem. A 6 (47) (2018) 23932–23977.

[46] X. Fan, et al., Fast and efficient preparation of exfoliated 2H MoS_2 nanosheets by sonication-assisted lithium intercalation and infrared laser-induced 1T to 2H phase reversion, Nano Lett. 15 (9) (2015) 5956–5960.

[47] G. Eda, H. Yamaguchi, D. Voiry, T. Fujita, M. Chen, M. Chhowalla, Photoluminescence from chemically exfoliated MoS_2, Nano Lett. 11 (12) (2011) 5111–5116.

[48] P. Blake, et al., Making graphene visible, Appl. Phys. Lett. 91 (6) (2007) 063124.

[49] X. Wang, K. Kang, S. Chen, E.H. Yang, Location-specific growth and transfer of arrayed MoS_2 monolayers with controllable size, 2D Mater. 4 (2017) 025093.

[50] J. Jeon, et al., Layer-controlled CVD growth of large-area two-dimensional MoS_2 films, Nanoscale 7 (5) (2015) 1688–1695.

[51] H. Xu, et al., Control of the nucleation density of molybdenum disulfide in large-scale synthesis using chemical vapor deposition, Materials (Basel) 11 (6) (2018) 870.

[52] E.Z. Xu, et al., p-Type transition-metal doping of large-area MoS_2 thin films grown by chemical vapor deposition, Nanoscale 9 (10) (2017) 3576–3584.

[53] K. Zhang, et al., Manganese doping of monolayer MoS_2: the substrate is critical, Nano Lett. 15 (10) (2015) 6586–6591.

[54] T. Hallam, et al., Rhenium-doped MoS_2 films, Appl. Phys. Lett. 111 (20) (2017) 203101.

[55] S. Das, M. Demarteau, A. Roelofs, Nb-doped single crystalline MoS_2 field effect transistor, Appl. Phys. Lett. 106 (17) (2015) 173506.

[56] Y. Kim, H. Bark, G.H. Ryu, Z. Lee, C. Lee, Wafer-scale monolayer MoS_2 grown by chemical vapor deposition using a reaction of MoO_3 and H_2 S, J. Phys. Condens. Matter 28 (18) (2016) 184002.

[57] H. Yu, et al., Wafer-scale growth and transfer of highly-oriented monolayer MoS_2 continuous films, ACS Nano 11 (12) (2017) 12001–12007.

[58] Q. Yu, J. Lian, S. Siriponglert, H. Li, Y.P. Chen, S.-S. Pei, Graphene segregated on Ni surfaces and transferred to insulators, Appl. Phys. Lett. 93 (11) (2008) 113103.

[59] A. Reina, et al., Growth of large-area single- and Bi-layer graphene by controlled carbon precipitation on polycrystalline Ni surfaces, Nano Res. 2 (6) (2009) 509–516.

[60] K.F. McCarty, P.J. Feibelman, E. Loginova, N.C. Bartelt, Kinetics and thermodynamics of carbon segregation and graphene growth on Ru(0001), Carbon N. Y. 47 (7) (2009) 1806–1813.

[61] J. You, M.D. Hossain, Z. Luo, Synthesis of 2D transition metal dichalcogenides by chemical vapor deposition with controlled layer number and morphology, Nano Converg. 5 (1) (2018) 26.

[62] J.D. Cain, F. Shi, J. Wu, V.P. Dravid, Growth mechanism of transition metal dichalcogenide monolayers: the role of self-seeding fullerene nuclei, ACS Nano 10 (5) (2016) 5440–5445.

[63] D. Zhou, H. Shu, C. Hu, L. Jiang, P. Liang, X. Chen, Unveiling the growth mechanism of MoS_2 with chemical vapor deposition: from two-dimensional planar nucleation to self-seeding nucleation, Cryst. Growth Des. 18 (2) (2018) 1012–1019.

[64] N. Imanishi, K. Kanamura, Z. Takehara, Synthesis of MoS_2 thin film by chemical vapor deposition method and discharge characteristics as a cathode of the lithium secondary battery, J. Electrochem. Soc. 139 (8) (1992) 2082.

[65] Y.-H. Lee, et al., Synthesis of large-area MoS_2 atomic layers with chemical vapor deposition, Adv. Mater. 24 (17) (2012) 2320–2325.

[66] W. Zhang, et al., CVD synthesis of $Mo_{(1-x)}W_xS_2$ and $MoS_{2(1-x)}$ Se_{2x} alloy monolayers aimed at tuning the bandgap of molybdenum disulfide, Nanoscale 7 (32) (2015) 13554–13560.

[67] K. Kang, K. Godin, E.H. Yang, The growth scale and kinetics of WS_2 monolayers under varying H_2 concentration, Sci. Rep. 5 (2015) 13205.

[68] S. Wang, et al., Shape evolution of monolayer MoS_2 crystals grown by chemical vapor deposition, Chem. Mater. 26 (22) (2014) 6371–6379.

[69] S.Y. Yang, G.W. Shim, S.-B. Seo, S.-Y. Choi, Effective shape-controlled growth of monolayer MoS_2 flakes by powder-based chemical vapor deposition, Nano Res. 10 (1) (2017) 255–262.

[70] J.S. Lee, et al., Wafer-scale single-crystal hexagonal boron nitride film via self-collimated grain formation, Science 362 (6416) (2018) 817–821.

[71] J. Nishizawa, T. Kurabayashi, Mechanism of gallium arsenide MOCVD, Vacuum 41 (4–6) (1990) 958–962.

[72] J. Nishizawa, On the reaction mechanism of GaAs MOCVD, J. Electrochem. Soc. 130 (2) (1983) 413.

[73] T. Institution of Electrical Engineers, S. Hattori, S. Sakai, M. Takeyasu, M. Umeno, Electron. Lett. 20 (22) (1984) [Institution of Electrical Engineers].

[74] K. Kang, et al., High-mobility three-atom-thick semiconducting films with wafer-scale homogeneity, Nature 520 (7549) (2015) 656–660.

[75] S.M. Eichfeld, et al., Highly scalable, atomically thin WSe_2 grown *via* metal–organic chemical vapor deposition, ACS Nano 9 (2) (2015) 2080–2087.

[76] B. Kalanyan, et al., Rapid wafer-scale growth of polycrystalline 2H-MoS_2 by pulsed metal–organic chemical vapor deposition, Chem. Mater. 29 (15) (2017) 6279–6288.

[77] M. Binnewies, R. Glaum, M. Schmidt, P. Schmidt, Chemical vapor transport reactions – a historical review, Zeitschrift für Anorg. und Allg. Chemie 639 (2) (2013) 219–229.

[78] D. Hu, et al., Two-dimensional semiconductors grown by chemical vapor transport, Angew. Chemie Int. Ed. 56 (13) (2017) 3611–3615.

[79] M. Dave, R. Vaidya, S.G. Patel, A.R. Jani, High pressure effect on MoS_2 and $MoSe_2$ single crystals grown by CVT method, Bull. Mater. Sci. 27 (2) (2004) 213–216.

[80] A. Ubaldini, J. Jacimovic, N. Ubrig, E. Giannini, Chloride-driven chemical vapor transport method for crystal growth of transition metal dichalcogenides, Cryst. Growth Des. 13 (10) (2013) 4453–4459.

[81] S. Tiefenbacher, H. Sehnert, C. Pettenkofer, W. Jaegermann, Epitaxial films of WS_2 by metal organic van der Waals epitaxy (MO-VDWE), Surf. Sci. 318 (1−2) (1994) L1161−L1164.

[82] Q. He, et al., Molecular beam epitaxy scalable growth of wafer-scale continuous semiconducting monolayer $MoTe_2$ on inert amorphous dielectrics, Adv. Mater. (2019) 1901578. Jun.

[83] R.F.C. Farrow, Molecular Beam Epitaxy: Applications to Key Materials, Noyes Publications, 1995.

[84] A. Koma, K. Saiki, Y. Sato, Heteroepitaxy of a two-dimensional material on a three-dimensional material, Appl. Surf. Sci. 41−42 (1990) 451−456.

[85] D. Fu, et al., Molecular beam epitaxy of highly crystalline monolayer molybdenum disulfide on hexagonal boron nitride, J. Am. Chem. Soc. 139 (27) (2017) 9392−9400.

[86] S. Sasaki, et al., Growth and optical properties of Nb-doped WS_2 monolayers, Appl. Phys. Express 9 (7) (2016) 071201.

[87] S.K. Pandey, H. Alsalman, J.G. Azadani, N. Izquierdo, T. Low, S.A. Campbell, Controlled p-type substitutional doping in large-area monolayer WSe_2 crystals grown by chemical vapor deposition, Nanoscale 10 (45) (2018) 21374−21385.

[88] M.R. Laskar, et al., p-type doping of MoS_2 thin films using Nb, Appl. Phys. Lett. 104 (9) (2014) 092104.

[89] S. Mouri, Y. Miyauchi, K. Matsuda, Tunable photoluminescence of monolayer MoS_2 via chemical doping, Nano Lett. 13 (12) (2013) 5944−5948.

[90] W.H. Chae, J.D. Cain, E.D. Hanson, A.A. Murthy, V.P. Dravid, Substrate-induced strain and charge doping in CVD-grown monolayer MoS_2, Appl. Phys. Lett. 111 (14) (2017) 143106.

[91] Y. Kim, H. Bark, B. Kang, C. Lee, Wafer-scale substitutional doping of monolayer MoS_2 films for high-performance optoelectronic devices, ACS Appl. Mater. Interfaces 11 (13) (2019) 12613−12621.

[92] F. Cadiz, et al., Excitonic linewidth approaching the homogeneous limit in MoS_2-based van der Waals heterostructures, Phys. Rev. X 7 (2) (2017) 021026.

[93] J. Gusakova, et al., Electronic properties of bulk and monolayer TMDs: theoretical study within DFT framework (GVJ-2e method), Phys. Status Solidi 214 (12) (2017) 1700218.

[94] S. Tongay, et al., Two-dimensional semiconductor alloys: monolayer $Mo_{1-x}W_xSe_2$, Appl. Phys. Lett. 104 (1) (2014) 012101.

[95] K. Zhang, et al., Tuning the electronic and photonic properties of monolayer MoS_2 via in situ rhenium substitutional doping, Adv. Funct. Mater. 28 (16) (2018) 1706950.

[96] J. Suh, et al., Doping against the native propensity of MoS_2: degenerate hole doping by cation substitution, Nano Lett. 14 (12) (2014) 6976−6982.

[97] H. Li, et al., Growth of alloy $MoS_{2x}Se_{2(1-x)}$ nanosheets with fully tunable chemical compositions and optical properties, J. Am. Chem. Soc. 136 (10) (2014) 3756−3759.

[98] X. Duan, et al., Synthesis of $WS_{2x}Se_{2-2x}$ alloy nanosheets with composition-tunable electronic properties, Nano Lett. 16 (1) (2016) 264−269.

[99] L. Yang, et al., Chloride molecular doping technique on 2D materials: WS_2 and MoS_2, Nano Lett. 14 (11) (2014) 6275−6280.

[100] A. Azcatl, et al., Covalent nitrogen doping and compressive strain in MoS_2 by remote N_2 plasma exposure, Nano Lett. 16 (9) (2016) 5437−5443.